Preprint Title The kinetic investigation of Zn3(OH)2V2O7•2H2O nanosheets at various conditions by In-situ Electrochemical Impedance Spectroscopy

Authors Qingwen Liu and haowen Liu

Article Type Full Research Paper

ORCID® iDs haowen Liu - https://orcid.org/0000-0001-7746-9593

The kinetic investigation of $Zn_3(OH)_2V_2O_7 \cdot 2H_2O$ nanosheets at various conditions by In-situ Electrochemical Impedance Spectroscopy

Qingwen Liu, Haowen Liu*

The college of chemistry and materials, South-Central University for Nationalities, Wuhan, 430074, PR China

Abstract In this paper, two dimensional nanosheet (2D) crystal, formulated as $Zn_3(OH)_2V_2O_7 \cdot 2H_2O$ has been synthesized by a facile hydrothermal method. Its crystal facet, morphology and structural evolutions of the resulting material are characterized with considerable temporal resolution. Applied for anode of lithium-half batteries, the powder that is thermally treated for approximately exhibits a rather high capacity, long-term cycling stability, and good rate capability due to intrinsically great surface area, the trimmed diffusion distance and probably synergetic effects of Zn and V ions. Furthermore, the in-situ electrochemical impedance spectra of ZVO-10 during the initial discharge–charge cycle are simulated based on the equivalent electrical circuit and the non-linear least square regression method. The results support the fact that the kinetics property changes, significantly, when discharged to 0.5 V, and then keeps stability in the charge.

Keywords Li-ion batteries; $Zn_3(OH)_2V_2O_7 \cdot 2H_2O$; Nanosheets; Electrochemical kinetic

1. Introduction

*Corresponding author Tel/Fax: +86 2767842752

E-mail address: liuhwchem@hotmail.com

Currently, one of the research priorities on Li-ion batteries is to improve its high capacity for meeting the demand in large-scale electric vehicles and smart grids. Among various strategies, scientists take care of seeking the higher capacities candidate materials to replace the commercial graphite anode (372 mAh g^{-1}). Such as Ti-based oxides, alloy-type compounds and transition metal oxides[1].

Transition metal vanadates oxides ($Zn_3(OH)_2V_2O_7 \cdot 2H_2O$) is an important mineral and has been widely applied in the fields of catalysts, electrochromic devices and chemical sensor, etc [2, 3]. Recently, $Zn_3(OH)_2V_2O_7 \cdot 2H_2O$ has also received the attentions of several research groups as potential anode materials for Li-ions batteries in terms of its rich sources, higher capacity and the peculiar layered sandwich-like crystal structure where Zn atoms occupy three of four octahedral sites in a close-packed layer of O atoms [4, 5]. Such an open structure-framework and expanded interlayer spacing were demonstrated to facilitate lithium intercalation/migration. For example, He et al. reported that $Zn_3(OH)_2V_2O_7 \cdot 2H_2O$ nanosheets showed a steady platform near 1.4 V during lithium storage process[6]. The capacities of microspheres and nanobelts synthesized by Zhang et al. were 619 and 749.8 mAh g^{-1} after 20 cycles at 20 mA g^{-1}[7, 8], respectively. Mai' team prepared $Zn_3(OH)_2V_2O_7 \cdot 2H_2O$ microflowers through liquid phase method, and achieved about 1287 mAh g^{-1} after 120 cycles at 200 mA g^{-1} [5]. With the further help of graphene networks, $Zn_3(OH)_2V_2O_7 \cdot 2H_2O$ nanoplates delivered an enhanced reversible capacity of 854 mAh g^{-1} after 400 cycles at 500 mA g^{-1} [9]. Wang et al. discussed the electrochemical reaction mechanism of $Zn_3(OH)_2V_2O_7 \cdot 2H_2O$ nanosheets during the first cycle[10]. However, these works were mainly focused on the

synthesis, coating, morphology regulation, structure and lithium storage capacity, etc. To our knowledge, the kinetic properties such as the diffusion coefficients of lithium ions and charge transfer resistance have not been documented, which plays a vital role on the electrochemical performances of material, especially the rate capacity. On the other hand, for transition metal oxides anode, the electrochemical performance of the first discharge-charge process is totally different from that of the subsequent cycles[(11)]. Some irreversible reactions happen, including the dissolution of active material, the electrolyte decomposition and the formation of solid electrolyte interface (SEI), which results into the big capacity loss, the lower columbic efficiency and the rate capacity. Therefore, it is necessary to investigate the kinetic properties of lithium ions in $Zn_3(OH)_2V_2O_7 \cdot 2H_2O$ during the first lithiation/delithiation process.

In this paper, 2D $Zn_3(OH)_2V_2O_7 \cdot 2H_2O$ was prepared by a facile hydrothermal method. The morphology and size evolution of the heated samples were observed under time-depend experiments. Benefiting from the unique 2D structure and probably synergetic effects of Zn and V ions, the as-synthesized nanosheets displayed an excellent electrochemical performance. Further, the impedance parameters as a function of voltage during the 1st cycle have been evaluated and interpreted in detail.

2. Experimental

All the used chemical reagents were of analytical grade. The reactions were carried out according the reported literature with minor modifications [(6)]. Typically, 1mmol V_2O_5 and 6 mmol NaOH were dissolved in 40 ml distilled water, then 3 mmol $Zn(NO_3)_2 \cdot 9H_2O$ and 2 g cetyltrimethylammonium bromide were added into the above

solution. After stirring for 10 min, the obtained white and viscous solution was transferred into a 50 mL Teflon-lined autoclave and kept at 180 ℃ for different time. At last, the cooled solution was centrifuged and washed three times with distilled water and absolute ethanol and dried at 80 ℃ in oven. The samples heated for 5, 10 and 24 h was denoted as ZVO-5, ZVO-10 and ZVO-24, respectively.

The crystalline phase and structure of the as-prepared powder was identified by Powder X-ray diffraction (XRD) analysis using Cu Kα radiation (λ=1.54056 Å) (Bruker D8-advance, Germany) at room temperature. The morphologies were investigated with field-emission scanning electron microscopy (FE-SEM, Hitachi, SU8010). Thermo gravimetric analysis (TGA) and deferential thermal analysis (DTA) were characterized on a NETZSCH 209F3 device (Germany). The heating rate was 10 °C min^{-1}. Raman spectrum was run on a DXRxi Raman Imaging microscope (U. S. A) under a 520 nm excitation laser. The two-electrode button cells were assembled in an argon-filled glove box. The counter electrode was lithium foil. The anode was the as-prepared sample mixed with 12% acetylene black and 8% polytetrafluoroethylene. The electrolyte was 1M $LiPF_6$ in a 1:1 (v/v) mixture of ethylene carbonate and dimethylcarbonate. The cell separator was Celgard 2300 membrane. All the electrical measurements were carried out by a battery testing system (CT2001A, 5 V/10 mA, Wuhan, China) at room temperature. The in situ Electrochemical impedance spectroscopes (EIS) experiment were performed in a Autolab PGSTAT302 electrochemistry workstation. The Nyquist plots were obtained at amplitude of 10 mV, and the frequency range applied was from 0.01 to 100 kHz.

3. Results and discussion

The phase, purity and structure of the obtained samples were characterized by powder XRD. As seen in Fig. 1, after 5 h of hydrothermal reaction, the obtained powder was a mixture with the predominant phase $Zn_3(OH)_2V_2O_7 \cdot 2H_2O$. As the reaction was prolonged to above 10 h, all diffraction peaks was sharp and matched well with the standard XRD pattern of hexagonal $Zn_3(OH)_2V_2O_7 \cdot 2H_2O$ (PDF#50-0570, blue lines in bottom), which showed that the pure $Zn_3(OH)_2V_2O_7 \cdot 2H_2O$ with better crystallinity was synthesized. It is noticed that all the diffraction peaks of ZVO-24 were shifted to the lower 2 θ angle, indicative of increase in interlayer distance (d_{hkl}) according to the Braggs law (Eq. (1)):

$$2d_{hkl} \sin\theta_{hkl} = \lambda \quad (1)$$

where λ is the X-ray wavelength (0.15406 nm) and θ_{hkl} is the diffraction angle. After refined with TOPSA 3.0 software according to space group ($P\bar{3}m1$), the obtained lattice parameters for ZVO-5, ZVO-10 and ZVO-24 was a=6.07 Å, c=7.17 Å; a=6.05 Å, c=7.15 Å and a=6.04 Å , c=7.18 Å , respectively, very close to the standard values (a= 6.05 Å, c=7.19 Å).

Furthermore, the crystalline size (D) on some selected lattice planes of the obtained samples had been calculated in terms of Scherrer formula (Eq. (2)). As listed in Table 1, the results showed that the smallest crystal size appeared on plane (001) for all the powders. No matter every plane crystal size or the average crystal size of all the samples, the biggest one appeared on ZVO-24.

$$D = K\lambda/\beta\cos\theta \quad (2)$$

where K =0.9 and β is full width at half-maximum.

Fig. 1b is Raman spectrum of ZVO-10. The profile was very similar to the reported[12]. The peak at 453.71 cm^{-1} can be assigned to Zn–O vibration peaks. The three peaks located at 488.42, 787.33 and 868.33 cm^{-1} comes from V–O band. Both peaks 214.58 and 251.22 cm^{-1} are originated from the related symmetry vibration. Fig. 1c is the thermal behavior analysis of ZVO-10 from room temperature to 700 ℃ in N_2 atmosphere. The total mass can be divided into two steps. The first loss with 9.9% from the ambient temperature to 234.2 ℃ is related to the evaporation of the absorbed water and the crystal water (Eq. (3)). Another 4.7% loss from 234.2 to 400 ℃ can be assigned to the decomposition reaction of $Zn_3(OH)_2V_2O_7 \cdot 2H_2O$, which is well agree with the theoretical value of 4.06% (Eq. (4))[13, 14]. The constant curve after 700 ℃ demonstrates than no any reactions happen.

$$Zn_3(OH)_2V_2O_7 \cdot 2H_2O \rightarrow Zn_3(OH)_2V_2O_7 + 2H_2O \quad (3)$$

$$Zn_3(OH)_2V_2O_7 \rightarrow Zn_3(VO_4)_2 + 2H_2O \quad (4)$$

Fig. 2 displayed the morphology and size evolution of the productions in the hydrothermal dwell time. In the 5 h reaction stage, an irregular 2D nanosheets with about 25 nm thickness (Fig. 2c) was observed. With the reaction going on (10 h), the thickness was increased to ~48 nm and some hexagonal particle emerged. After the reaction time reached 24 h, the thickness was increased to about 1.5 um (Fig. 2d). The result of SEM investigation was accordance with the above XRD data, which can be explained based on the Ostwald ripening and growth mechanism [15]. Combined with XRD analysis and the previous report[10], it can be referred that facts vertical to the 2D plane is (001). All the particles for ZVO-24 showed a well defined regular hexagonal

and the surface became more smooth, which was stemmed from the inherent anisotropic nature of $Zn_3(OH)_2V_2O_7 \cdot 2H_2O$ [7, 14].

Fig. 3a presents the first three discharge and charge curves of the obtained samples at 1.0 A g^{-1} in 0.01-3.0 V. The open circuit voltage (OCV) of the fresh cell was about 2.85 V. The voltage profiles are indicative of typical lithium storage characteristics of $Zn_3(OH)_2V_2O_7 \cdot 2H_2O$[5, 10]. During the initial discharge, the quick decreased process from 2.85 to 0.70 V can be assigned to the irreversible lithium insertion (Eq. (5)). The first voltage that appears at ~0.75 V is associated with the decomposition of $Li_{1+x}Zn_3V_2O_7(OH)_2 \cdot 2H_2O$ (Eq. (6)). The second long flat at~0.6 V, delivered the major capacity, can be attributed to the alloying reaction between ZnO and LiZn and lithiation/delithiation of the lithium vanadate (Eq. (7-8)). The later slope can be related to the reaction between the active material with the electrolyte resulting into the formation of a SEI layer[5].

$$Zn_3V_2O_7(OH)_2 \cdot 2H_2O + xLi^+ + xe^- \rightarrow Li_{1+x}Zn_3V_2O_7(OH)_2 \cdot 2H_2O \quad (5)$$

$$Li_{1+x}Zn_3V_2O_7(OH)_2 \cdot 2H_2O \rightarrow Li_{1+x}V_2O_5 + ZnO + Li_2O + LiOH \quad (6)$$

$$ZnO + 3Li^+ + 3e^- \leftrightarrow LiZn + Li_2O \quad (7)$$

$$Li_{1+x}V_2O_5 \leftrightarrow LiV_2O_5 + xLi^+ + xe^- \quad (8)$$

The similar profile between the second and third cycle demonstrated the stable lithium uptake/release process. The upshift of the discharge potential and the downshift of the charge potential along with cycling were stemmed from the polarization. The initial coulombic efficiency (the ratio of the charge/discharge capacity) was only 85.6%. The bigger capacity loss of 250.2 mAh g^{-1} was originated from the irreversible formation of

$Li_{1+x}Zn_3V_2O_7(OH)_2 \cdot 2H_2O$ and SEI, companied with some undecomposed Li_2O phase[16].

Fig. 3b depicted the cycling performances of the as-prepared samples in 0.01-3.0 V at 1.0 A g^{-1}. All the samples displayed a quick capacity fading in the first several cycles, which is common phenomenon in the metal oxides[5]. ZVO-5 showed the worst cycling performance, which may be ascribed to the mixed-phase and the more side reactions. The initial discharge capacities were 1801.3 mAh g^{-1} for ZVO-5, 1734.6 mAh g^{-1} for ZVO-10 and 1317.9 mAh g^{-1} for ZVO-24. The probably synergetic effects of Zn and V ions was believed to responsible for the higher capacity[5]. The decreasing tendency in capacity can be attributed to the different surface area affording active intercalation sites[17, 18]. Comprised to ZVO-24 (392.6 mAh g^{-1}), ZVO-10 displayed the higher capacity (546.1 mAh g^{-1}) and the better cycling stability after 100 cycles, which can be attributed to the much thinner thickness than the microplates (~48 nm nm vs. 1.48 um). This can be further confirmed by another significant feature of the rate capacity (Fig. 3c). The ZVO-10 delivered discharge capacity of ~803, 378, 204 and 97 mAh g^{-1}, at the current densities of 1.0, 2.0, 5.0 and 10A g^{-1}, respectively. All of capacities were higher than that of ZVO-24 under the same tested conditions. Two factors were responsible for the enhanced lithiation/delithiationreaction kinetics. The larger surface area was favorable for Li^+ flux across the electrolyte/electrode interface. In addition, the diffusion distance of Li^+ ion can be reduced to a great extend by going into lower dimension which improves the electrochemical kinetics [18, 19].

The in situ EIS experiments were carried out to elucidate the change in the

electrochemical kinetics of the as-prepared ZVO-10 during the 1st discharge–charge process at a current rate of 1.0 A g^{-1}. The collected EIS data are shown in Fig. 4. Speaking generally, the typical Nyquist plot composed of two semi circles, one in the higher frequency range, another in the high to the moderate frequency zone, and an inclined line at low frequency region. The high frequency semicircle is related to Li^+ migration through the SEI layer (R_{sei}).The medium frequency semicircle can be ascribed to the resistance (R_{ct}) of charge transfer process at the electrode/electrolyte interface. The inclined line is referred to ionic diffusion in the active materials (Warburg impedance). When discharged from the OCV condition to 1.0 V, the Nyquist plot displayed a single semicircle in the range 100k ~4.0 Hz, which could be due to improper wetting of the electrode by the electrolyte[20]. As discharged to 0.5 V, the first-semicircle reduced significantly, the second semicircle emerged at moderate frequency region and did not disappear upon later cycles, which revealed that the passive film forms mostly when discharged to 0.5 V and existed during the latter cycles[21]. Also, the radiuses of the semicircles increased with the charge proceeding. According to the equivalent circuit (the insert in Fig. 4a, c) which consists of a series and parallel combination of resistances, corresponding constant phase elements (CPEs) and Warburg impedance Q_d, the fitted kinetics parameters at different state are listed in Table 2. The R_{sei} value firstly decreased from 108 Ω at the discharged 0.5 V to 71 Ω at the charged 0.3 V , then increased with charging went on, indicating the SEI film experienced a complex formation-dissolving-reformation process[22]. The R_{ct} of the cells firstly showed a slow down but then suddenly decreased at 0.5 V, implying a better charge transfer kinetics

and ascribed to the electrochemical active behavior[23]. Simultaneously the R_s value began to increase at 0.5 V, which can be ascribed to the electrolyte decomposition and its reactions with active material. All these demonstrated that the complex reactions occurred at 0.5 V. In addition, it should be noticed that the low frequency line in charge process became more obviously inclined towards the real axis than that discharge, which can be attributed to an increase of grain boundaries, resulting into slow Li-ion diffusion[24]. The Warburg factor (σ) is inversely proportional to the diffusion coefficient of Li-ion[25], which can be calculated from the slope of line between Z' and $\omega^{-1/2}$ (Fig. 4b, d).The smaller σ implied the better electrochemical kinetic. Hence, the kinetics property of ZVO-10 increased in the discharge process, and kept stability in the charge due to the close σ, Rct and Re values in charge process, indicating a highly stable Li-ion diffusion process.

4. Conclusions

In summary, 2D $Zn_3(OH)_2V_2O_7{\cdot}2H_2O$ was prepared by a facile hydrothermal reaction. The morphology and size of the samples were investigated with controlling the heat time. The results showed that 10 h would be sufficient for synthesizing $Zn_3(OH)_2V_2O_7{\cdot}2H_2O$. the relation between the structure and lithium storage performance was studied. Benefit from the large surface and super thin characteristics, the 10 h reaction samples delivered an excellent electrochemical performances. The in situ EIS technique has been employed to investigate the kinetics changes of ZVO-10 anode during the first discharge-charge process. the SEI film formed when discharged to 0.5 V and later experienced a complex formation-dissolving-reformation process.

References

1. J. Hassoun and B. Scrosati, *J Electrochem Soc*, **162**, A2582 (2015).
2. R. Shi, Y. J. Wang, F. Zhou and Y. F. Zhu, *J Mater Chem*, **21**, 6313 (2011).
3. A. Bayat, A. R. Mahjoub and M. M. Amini, *J Mater Sci-Mater El*, **29**, 2915 (2018).
4. P. Y. Zavalij, Z. Fan and M. Stanley, *Acta Cryst*, **C53**, 1738 (1997).
5. H. W. Yan, Y. Z. Luo, X. Xu, L. He, J. Tan, Z. H. Li, X. F. Hong, P. He and L. Q. Mai, *Acs Appl Mater Inter*, **9**, 27707 (2017).
6. S. B. Ni, G. Zhou, S. M. Lin, X. H. Wang, Q. T. Pan, F. Yang and D. Y. He, *Mater Lett*, **63**, 2459 (2009).
7. S. Y. Zhang, X. Xiao, M. Lu and Z. Q. Li, *J Mater Sci*, **48**, 3679 (2013).
8. S. Y. Zhang, N. Lei, W. Q. Ma, Z. Z. Zhang, Z. B. Sun and Y. J. Wang, *Mater Lett*, **129**, 91 (2014).
9. Y. Yu, C. J. Niu, C. H. Han, K. N. Zhao, J. S. Meng, X. M. Xu, P. F. Zhang, L. Wang, Y. Z. Wu and L. Q. Mai, *Ind Eng Chem Res*, **55**, 2992 (2016).
10. G. Z. Yang, S. Y. Li, M. M. Wu and C. X. Wang, *J Mater Chem A*, **4**, 10974 (2016).
11. J. Jin, L. Wu, S. Huang, M. Yan, H. Wang, L. Chen, T. Hasan, Y. Li and B.-L. Su, *small*, **2**, 1800171 (2018).
12. S. B. Ni, X. H. Wang, X. L. Sun, F. Yang, Y. Q. Liu and D. Y. He, *Mater Chem Phys*, **124**, 803 (2010).
13. M. Wang, Y. J. Shi and G. Q. Jiang, *Mater Res Bull*, **47**, 18 (2012).
14. F. F. Wang, W. B. Wu, X. J. Sun, S. Y. Song, Y. Xing, J. W. Wang, D. H. Yu and Z. M. Su, *Mater Charact*, **86**, 139 (2013).
15. A. X. Wang, X. J. Hu, F. Wang, W. Chen, Y. P. Pang, S. Javaid, D. C. Chen, X. Y. Li, L. Staaden and G. H. Jia, *Mater Lett*, **237**, 88 (2019).
16. Y. Li, L. B. Kong, M. C. Liu, W. B. Zhang and L. Kang, *Ceram Int*, **43**, 1166 (2017).
17. L. H. Li, C. Y. Nan, J. Lu, Q. Peng and Y. D. Li, *Chem Commun*, **48**, 6945 (2012).
18. X. D. Liu, G. Y. Liu, L. J. Wang, Y. P. Li, Y. P. Ma and J. M. Ma, *J Power Sources*, **312**, 199 (2016).
19. K. T. Lee and J. Cho, *Nano Today*, **6**, 28 (2011).
20. A. K. Rai, L. T. Anh, J. Gim and J. Kim, *Ceram Int*, **39**, 9325 (2013).
21. J. S. Zhao, L. Wang, X. M. He, C. R. Wan and C. Y. Jiang, *Int J Electrochem Sc*, **5**, 478 (2010).
22. S. Khalid, C. B. Cao, M. Naveed and W. Younas, *Sustain Energ Fuels*, **1**, 1795 (2017).
23. A. K. Rai, T. V. Thi, B. J. Paul and J. Kim, *Electrochim Acta*, **146**, 577 (2014).
24. U. K. Sen and S. Mitra, *Rsc Adv*, **2**, 11123 (2012).
25. J. Leng, Z. X. Wang, X. H. Li, H. J. Guo, H. K. Li, K. M. Shih, G. C. Yan and J. X. Wang, *J Mater Chem A*, **5**, 14996 (2017).

Table 1. The calculated lattice constants and crystal size.

Samples	crystal size (nm)						Average size (nm)	lattice constants (Å)		Rwp (%)
	(001)	(010)	(011)	(002)	(010)	(012)		a	c	
ZVO-5	17.8	53.1	25.4	36.3	43	20	28.0	6.07	7.17	4.8
ZVO-10	38.2	60.1	45.7	48.3	52.6	42.7	60.7	6.05	7.15	8.7
ZVO-24	43.5	73.2	49.1	72.2	47	46	73.6	6.04	7.18	6.4

Table 2. Impedance evolution of ZVO-10 battery during the 1st cycle

State (V)	Discharge				Charge			
	Rs (Ω)	Rsei (Ω)	Rct (Ω)	σ	Rs (Ω)	Rsei (Ω)	Rct (Ω)	σ
0.5	10.8	108	44.9	41.71	12.1	71	21.5	2.92
1.0	6.51	-	368	89.24	15.2	92	22.3	4.64
1.3	6.3	-	401	98.39	16.6	101	27.8	6.86
Fresh	7.04	-	453	97.89	-	-	-	-

The list of figure captions:

Fig. 1 (a)XRD patterns of the obtained samples, (b) Raman spectra and (c) TG and DTA analysis of ZVO-10.

Fig. 2 SEM images at different magnifications of the as-prepared samples (a, b, c) for ZVO-5, (d, e, f) for ZVO-10 and (g, h, i) for ZVO-24.

Fig. 3 (a) the selected discharge-charge curves of ZVO-10 at 1.0 A g^{-1}, (b) the cycling performance of the as-prepared samples at 1.0 A g^{-1}, and (c) the discharge capacity vs cycle number of ZVO-10 and ZVO-24 at a different current density in 0.1-3.0 V.

Fig. 4 (a, c) the Nyquist plots and (b, d) the corresponding graph of Z' plotted against $\omega^{-1/2}$ for ZVO-10 electrodes at different states during the first cycle. (the insert is the equivalent circuit).

Fig. 1

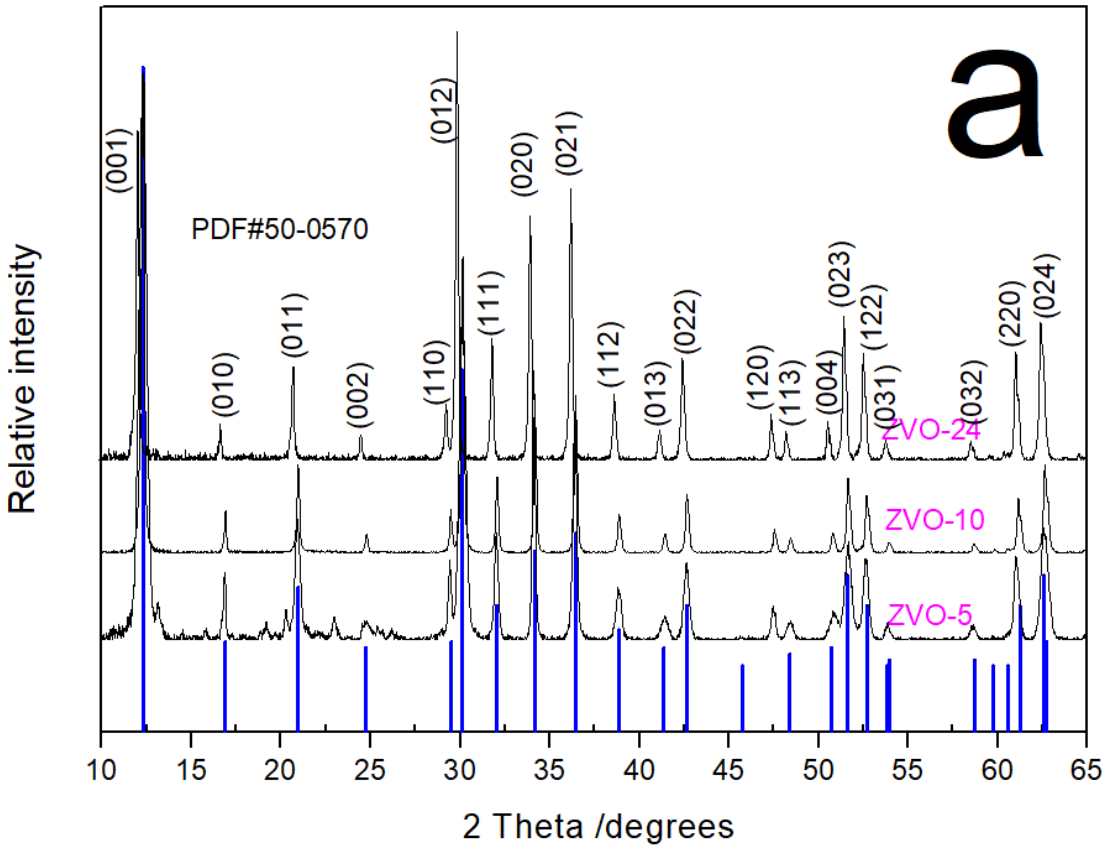
a
Relative intensity
PDF#50-0570
(001)
(010)
(011)
(002)
(110)
(012)
(111)
(020)
(021)
(112)
(013)
(022)
(120)
(113)
(004)
(023)
(122)
(031)
(032)
(220)
(024)
ZVO-24
ZVO-10
ZVO-5
10 15 20 25 30 35 40 45 50 55 60 65
2 Theta /degrees

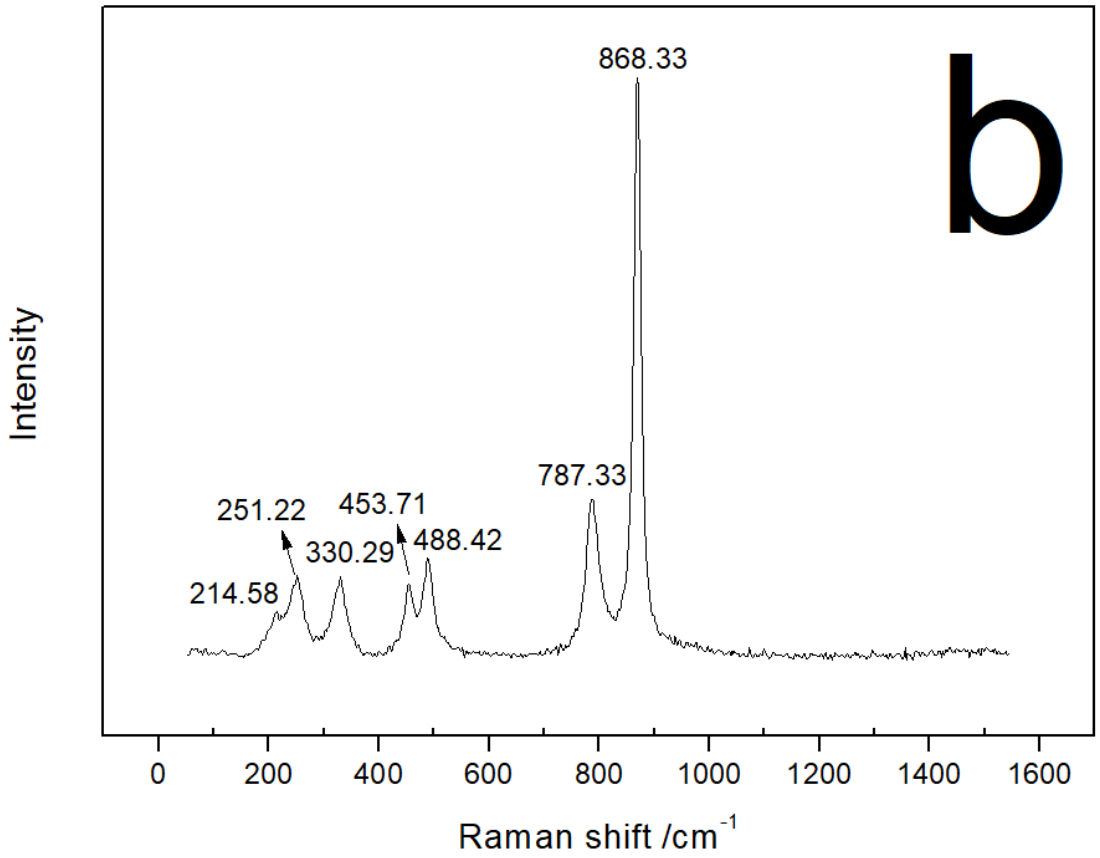
b
Intensity
868.33
787.33
251.22
453.71
330.29
488.42
214.58
0 200 400 600 800 1000 1200 1400 1600
Raman shift /cm-1

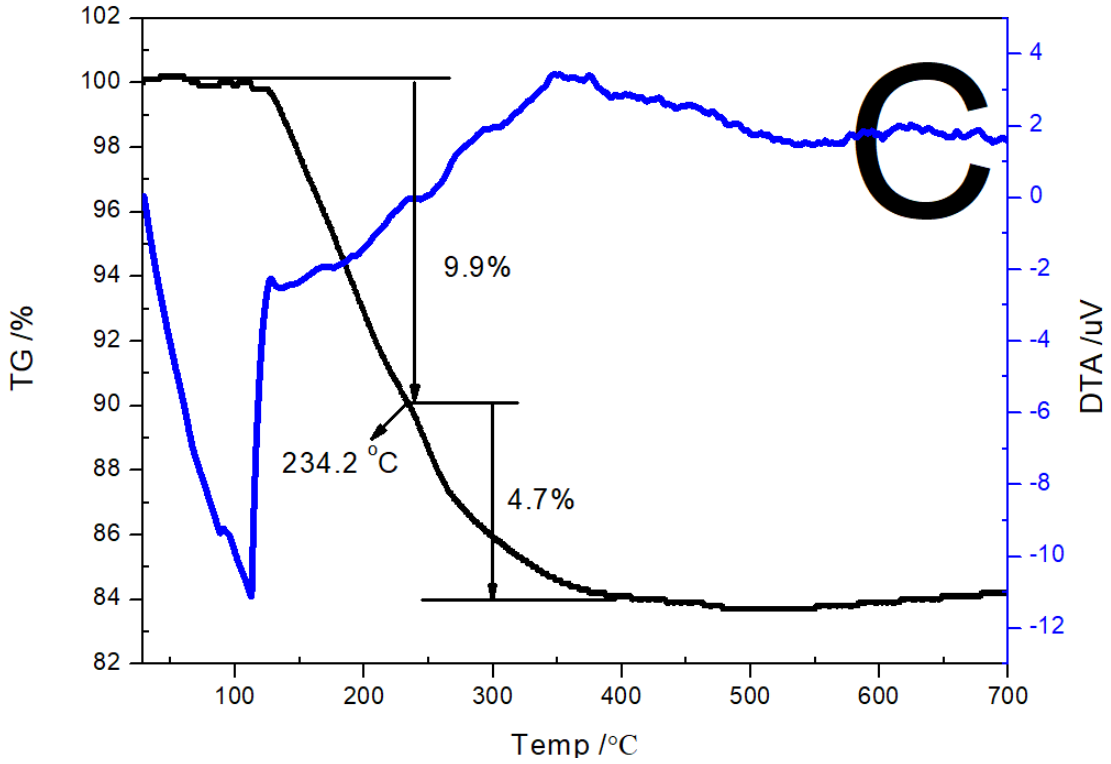
C
9.9%
234.2 °C
4.7%
TG /%
DTA /uV
Temp /°C
102
100
98
96
94
92
90
88
86
84
82
4
2
0
-2
-4
-6
-8
-10
-12
100
200
300
400
500
600
700

Fig. 2

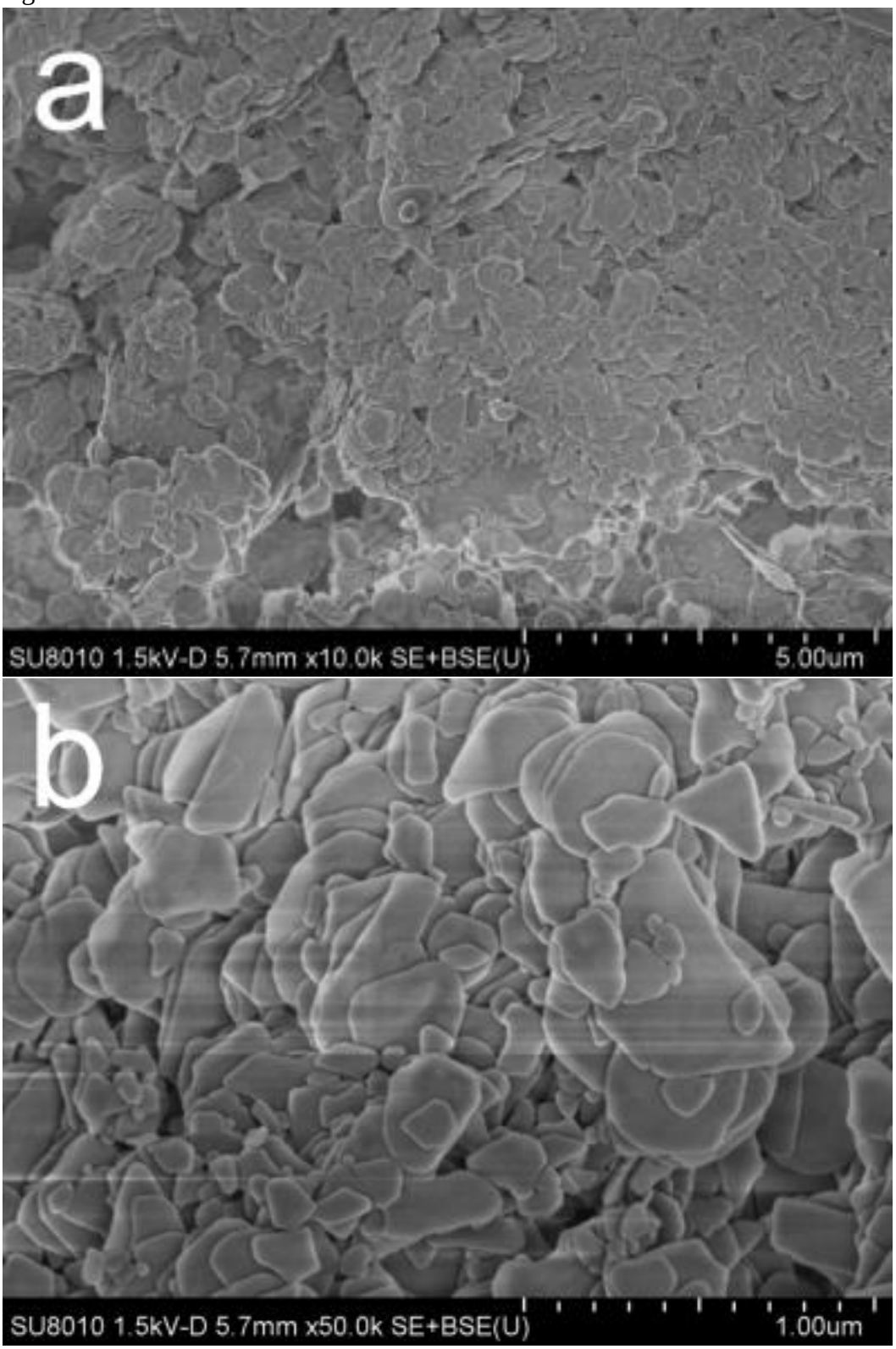
a
SU8010 1.5kV-D 5.7mm x10.0k SE+BSE(U)
5.00um
b
SU8010 1.5kV-D 5.7mm x50.0k SE+BSE(U)
1.00um

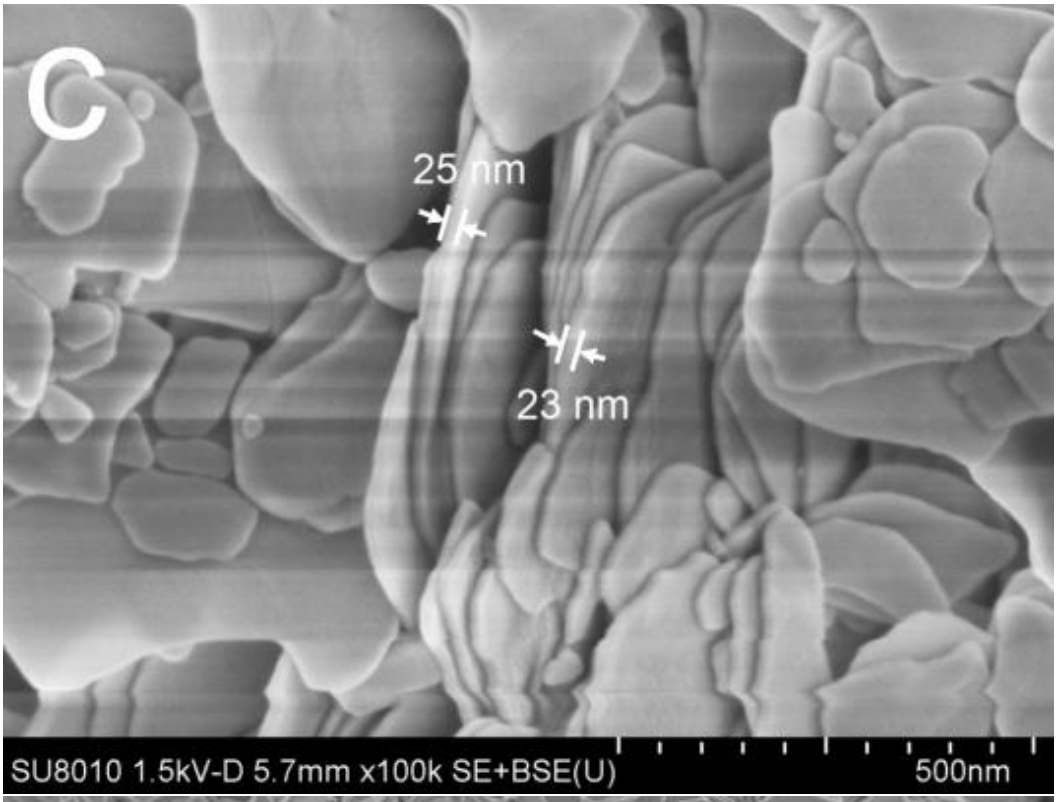
c
25 nm
23 nm
SU8010 1.5kV-D 5.7mm x100k SE+BSE(U)
500nm

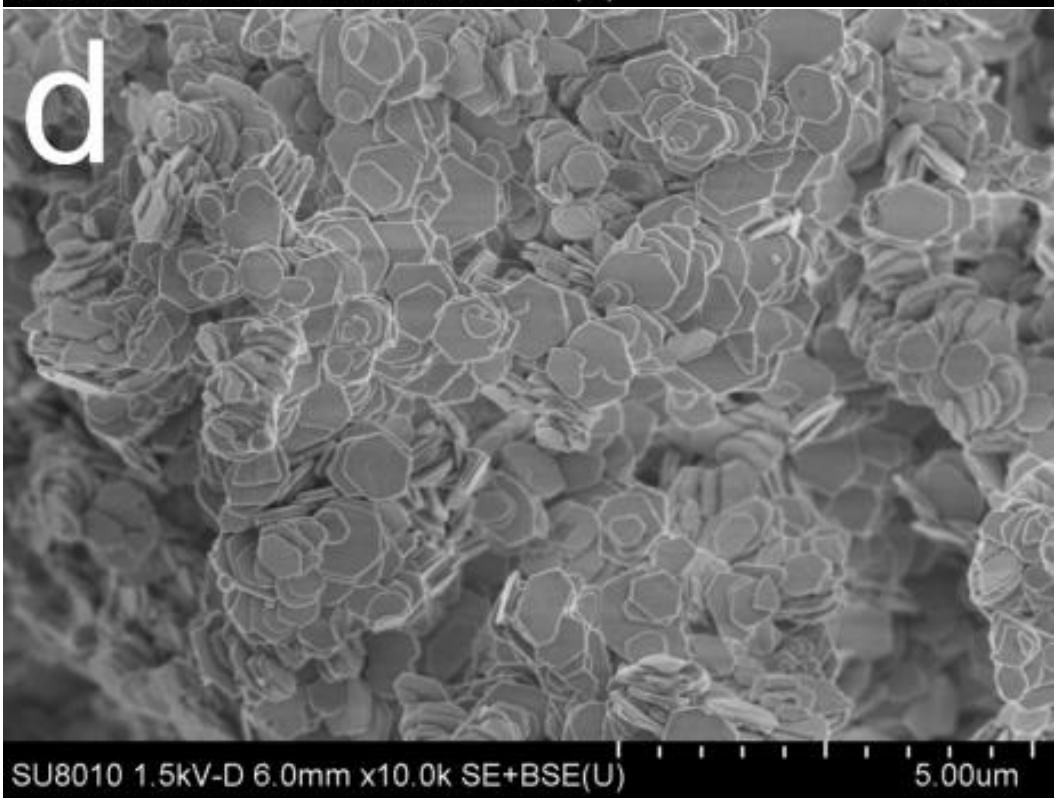
d
SU8010 1.5kV-D 6.0mm x10.0k SE+BSE(U)
5.00um

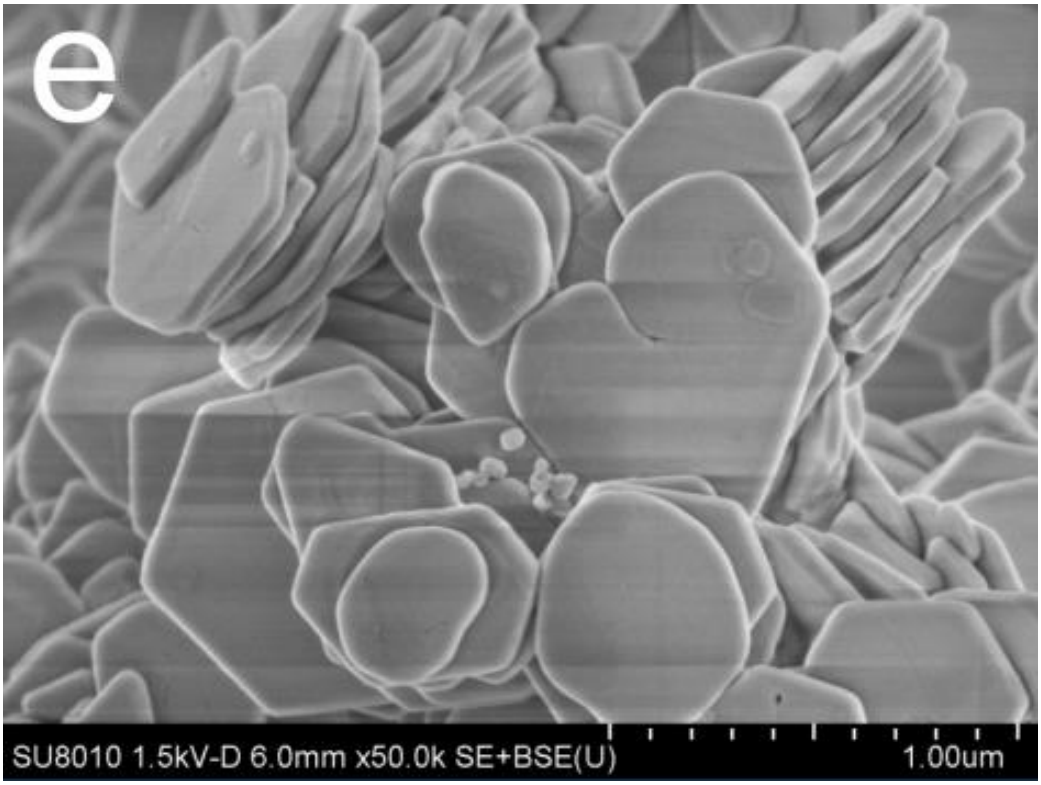
e
SU8010 1.5kV-D 6.0mm x50.0k SE+BSE(U)
1.00um

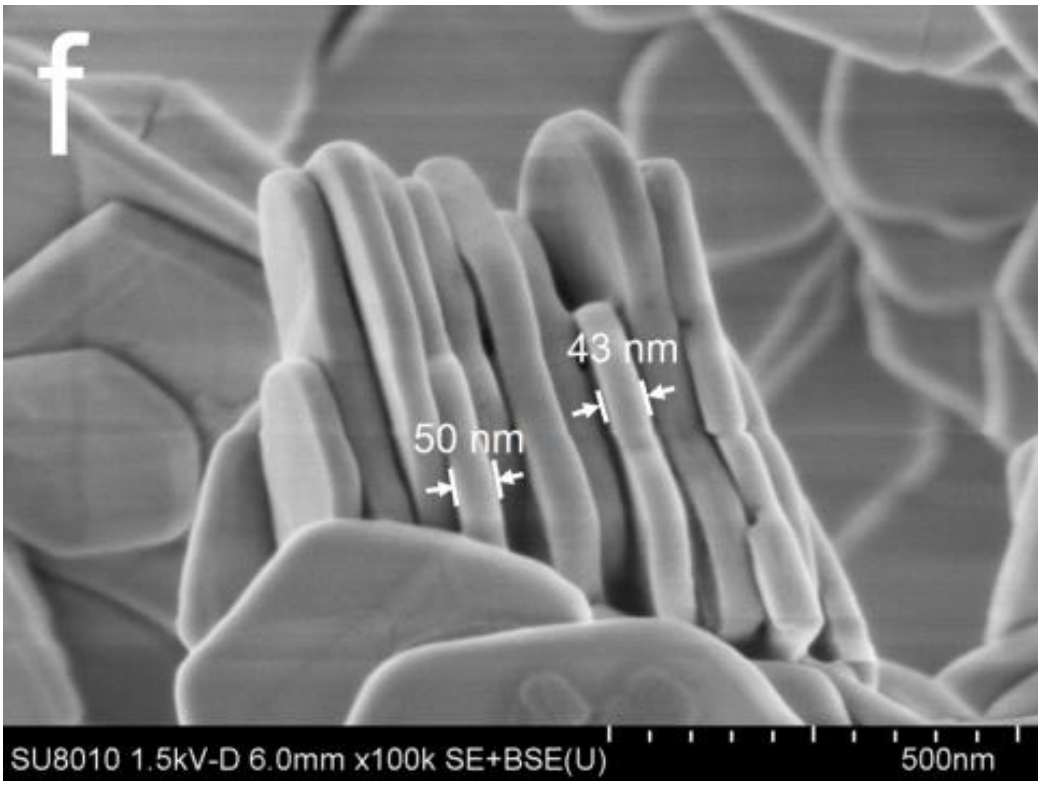
f
43 nm
50 nm
SU8010 1.5kV-D 6.0mm x100k SE+BSE(U)
500nm

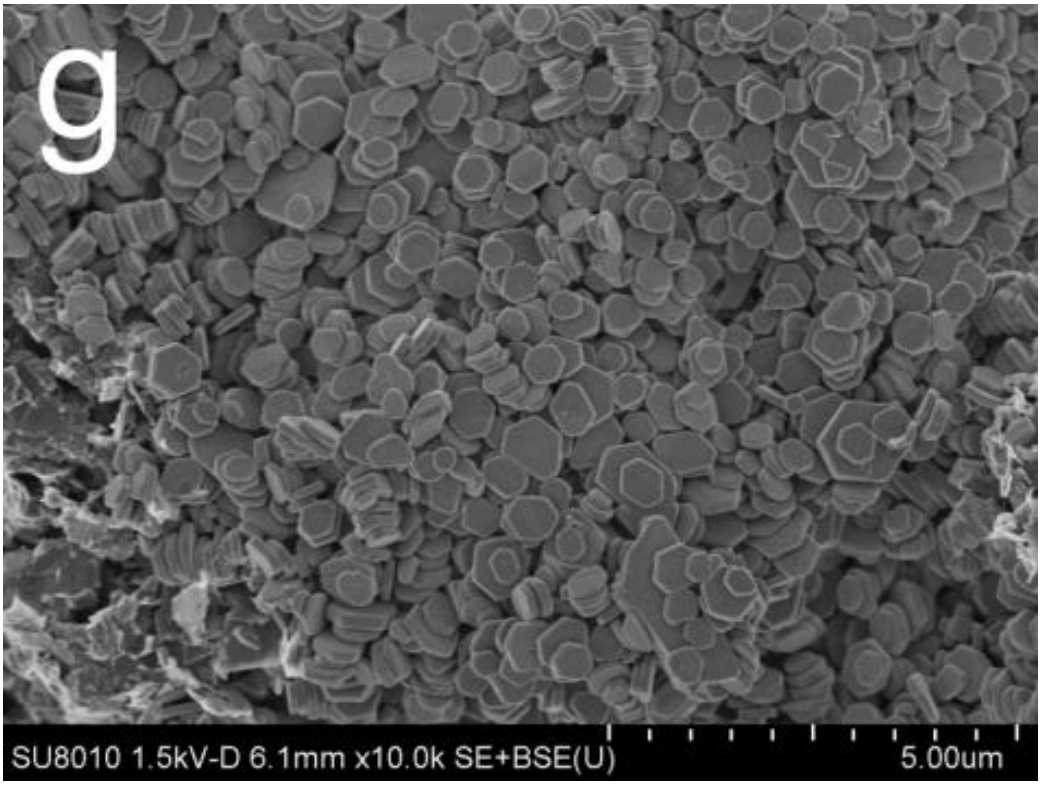
g
SU8010 1.5kV-D 6.1mm x10.0k SE+BSE(U)
5.00um

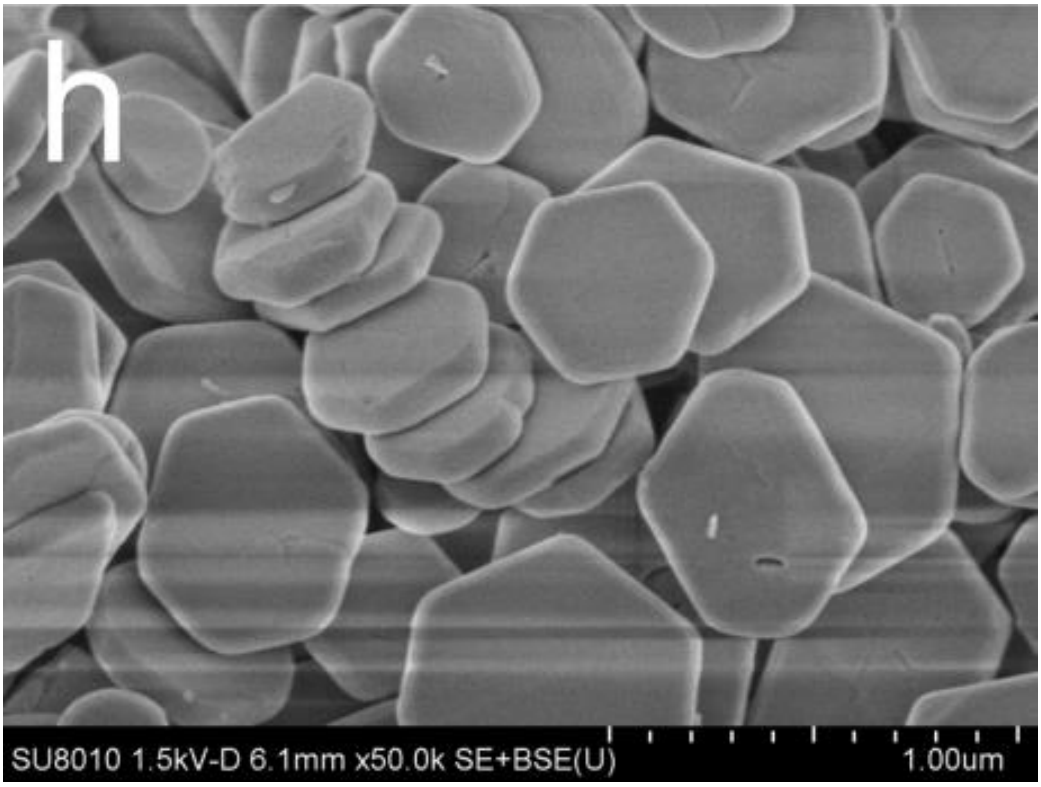
h
SU8010 1.5kV-D 6.1mm x50.0k SE+BSE(U)
1.00um

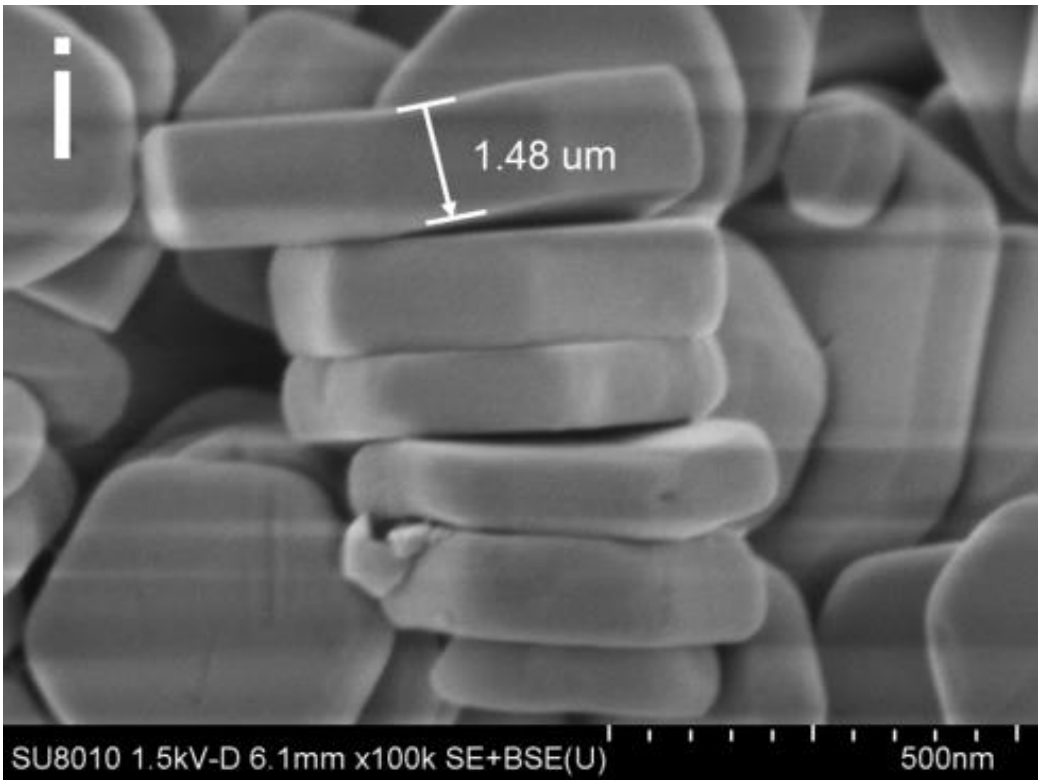
i
1.48 um
SU8010 1.5kV-D 6.1mm x100k SE+BSE(U)
500nm

Fig. 3

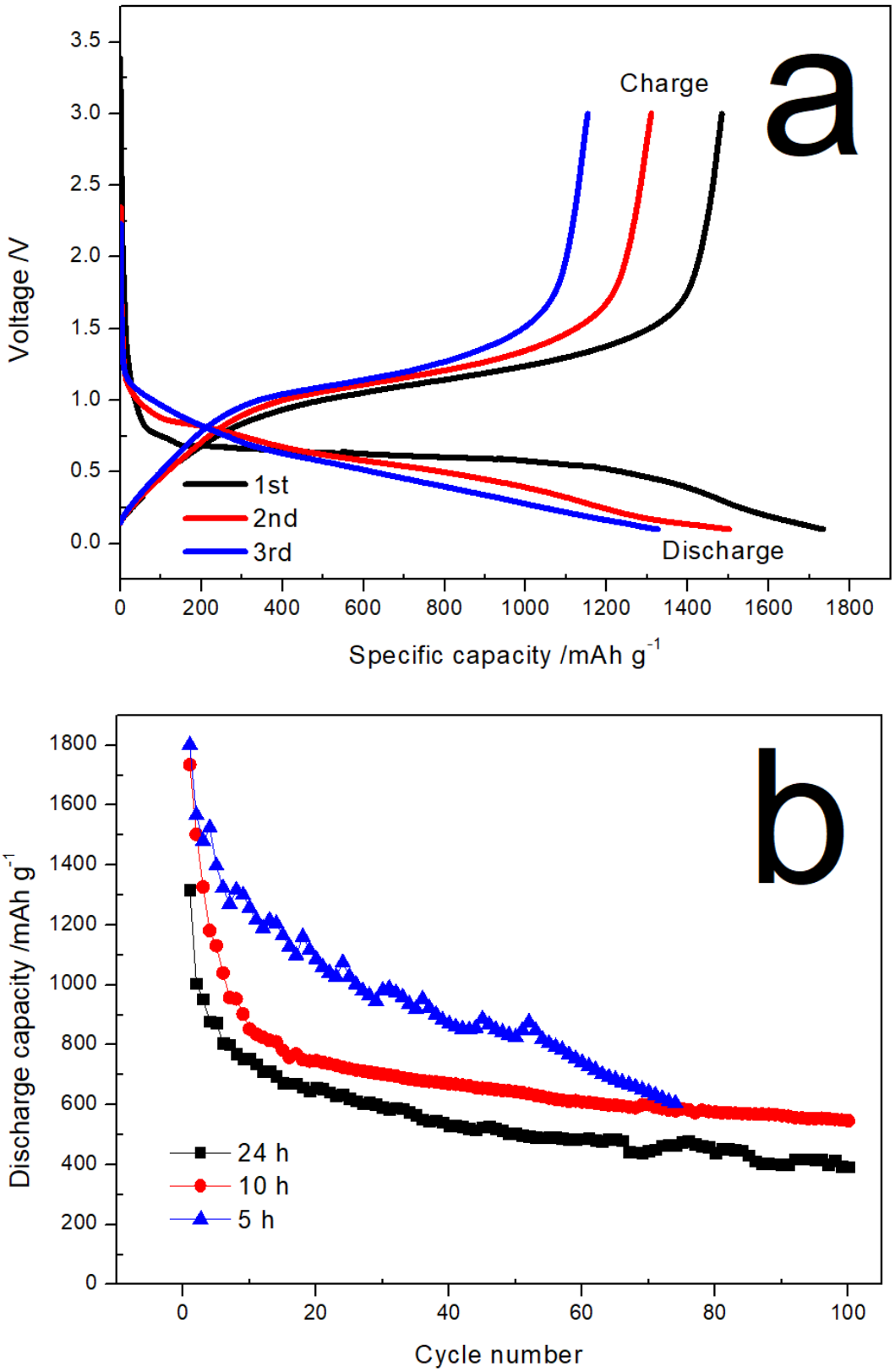
a
Charge
Discharge
1st
2nd
3rd
Voltage /V
Specific capacity /mAh g-1
b
24 h
10 h
5 h
Discharge capacity /mAh g-1
Cycle number

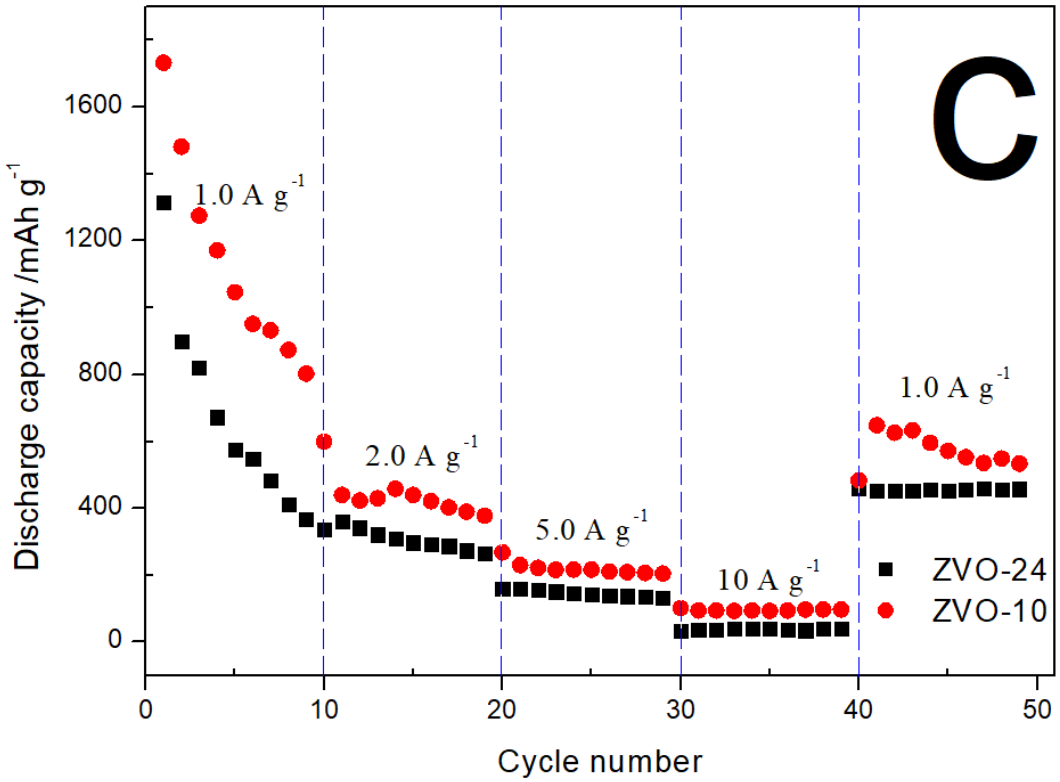
C
Discharge capacity /mAh g-1
Cycle number
1.0 A g-1
2.0 A g-1
5.0 A g-1
10 A g-1
1.0 A g-1
ZVO-24
ZVO-10
0
400
800
1200
1600
0
10
20
30
40
50

Fig. 4

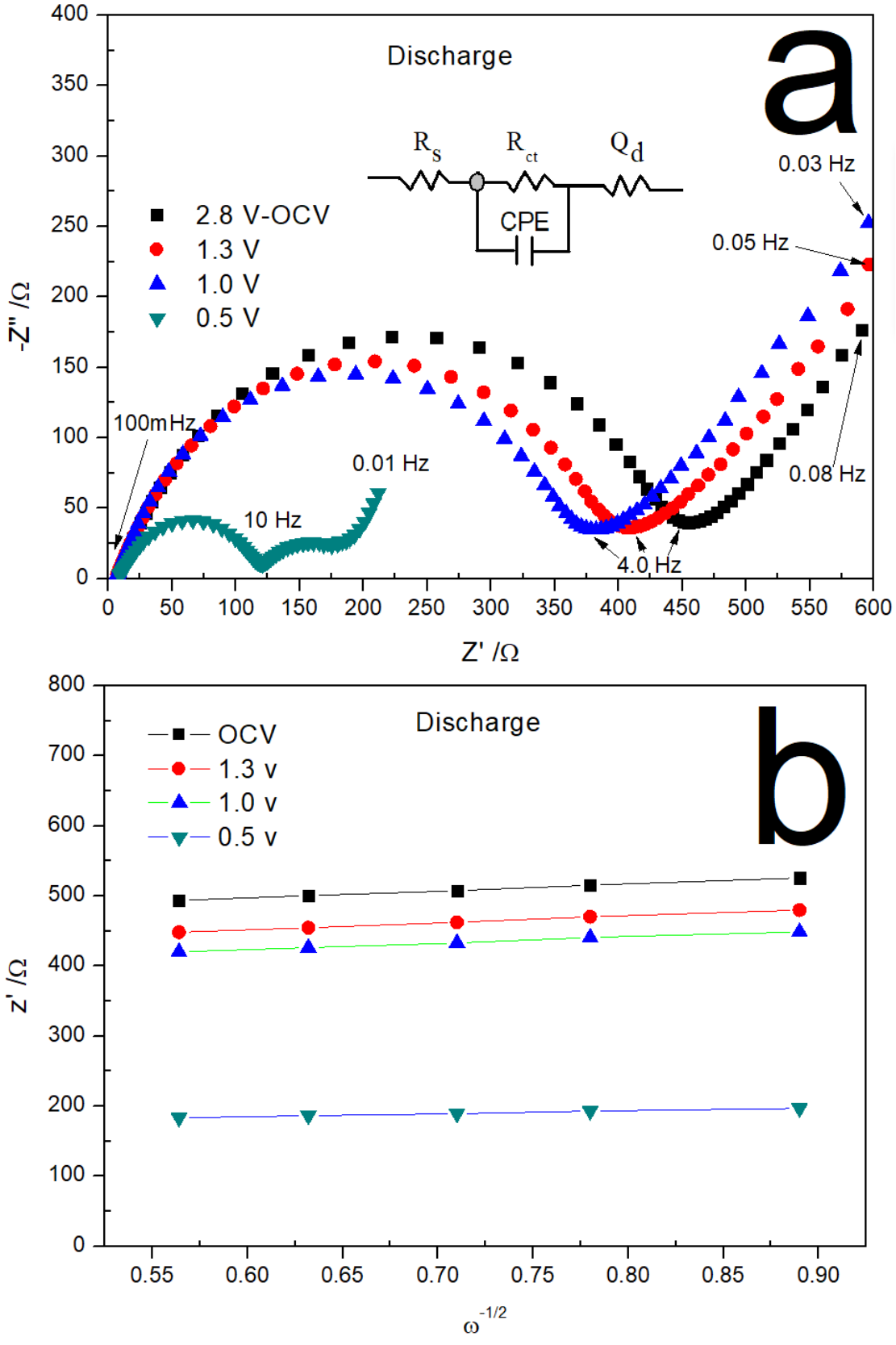
Discharge
a
R_s
R_{ct}
Q_d
CPE
2.8 V-OCV
1.3 V
1.0 V
0.5 V
0.03 Hz
0.05 Hz
100mHz
0.01 Hz
10 Hz
0.08 Hz
4.0 Hz
-Z'' /Ω
Z' /Ω
Discharge
b
OCV
1.3 v
1.0 v
0.5 v
z' /Ω
$\omega^{-1/2}$

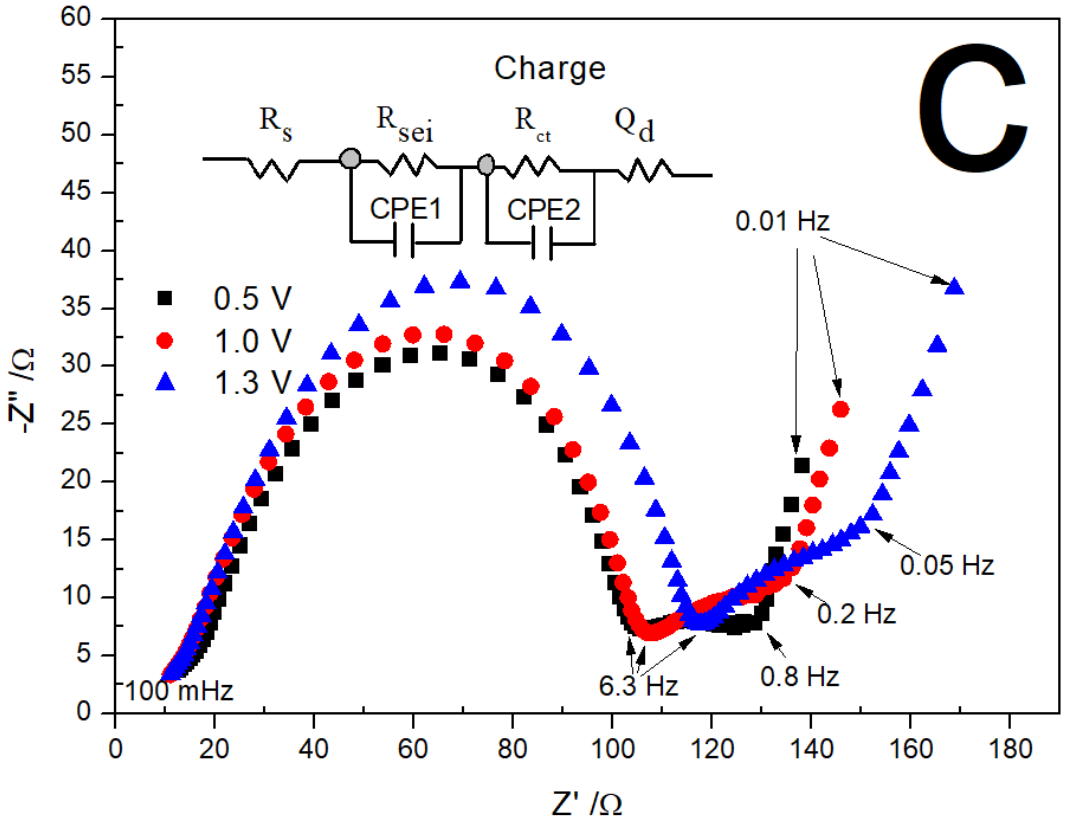
Charge
C
R_s
R_{sei}
R_{ct}
Q_d
CPE1
CPE2
0.5 V
1.0 V
1.3 V
0.01 Hz
0.05 Hz
0.2 Hz
0.8 Hz
6.3 Hz
100 mHz
-Z'' /Ω
Z' /Ω

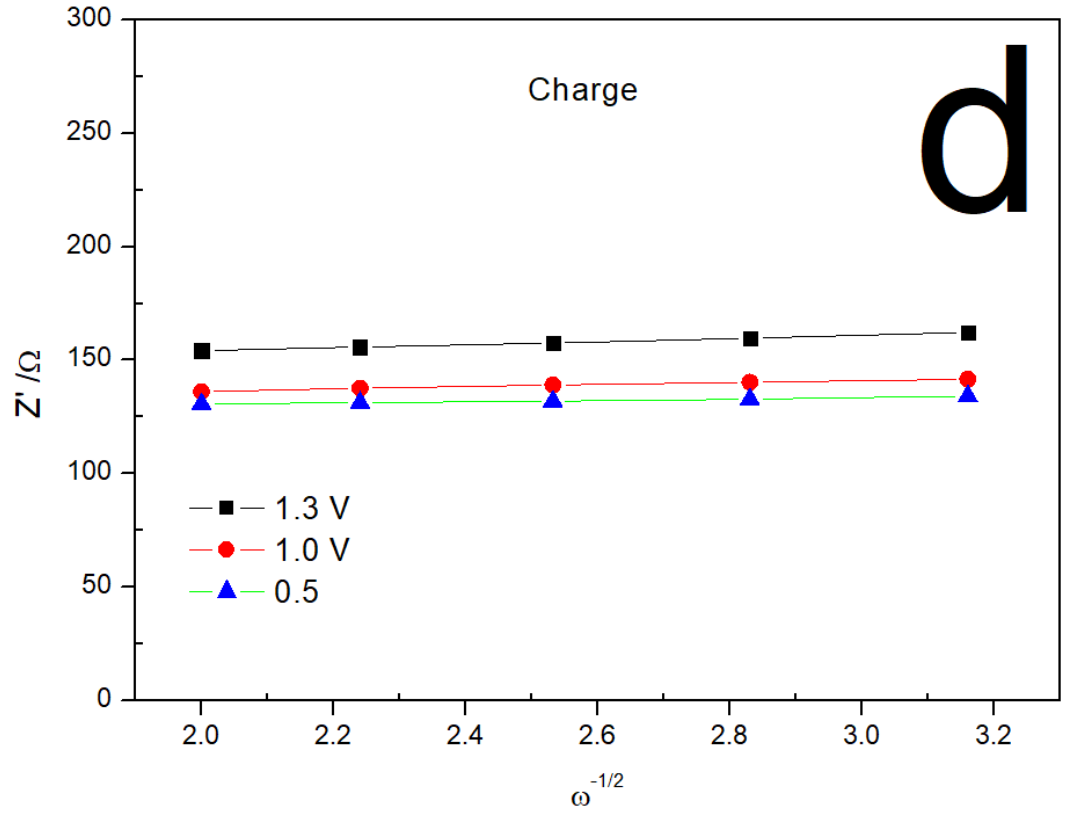
Charge
d
1.3 V
1.0 V
0.5
Z' /Ω
$\omega^{-1/2}$